

# Continuous transformations of cubic minimal surfaces

 A. Fogden<sup>1,a</sup> and S.T. Hyde<sup>2</sup>
<sup>1</sup> Physical Chemistry 1, Center for Chemistry and Chemical Engineering, University of Lund, Box 124, 221 00 Lund, Sweden

<sup>2</sup> Department of Applied Mathematics, Research School of Physical Sciences and Engineering, Canberra ACT 0200, Australia

Received: 5 March 1998 / Revised: 29 July 1998 / Accepted: 31 July 1998

**Abstract.** Although the primitive ( $P$ ), diamond ( $D$ ) and gyroid ( $G$ ) minimal surfaces form the structural basis for a multitude of self-assembling phases, such as the bicontinuous cubics, relatively little is known regarding their geometrical transformations, beyond the existence of the Bonnet isometry. Here their highest symmetry deformation modes, the rhombohedral and tetragonal distortions, are fully elucidated to provide a unified description of these simplest minimal surface families, with all quantities expressed in terms of complete elliptic integrals. The rhombohedral distortions of the gyroid are found to merge continuously with those which bridge the  $P$  and  $D$  surfaces, furnishing direct transformations between all three cubics, preserving both topology and zero mean curvature throughout. The tetragonal distortions behave analogously, offering an alternative route from the gyroid to the  $D$  surface. The cell axis ratios, surface areas and Gaussian curvature moments of all families are given, supplying the necessary geometrical input to a curvature energy description of cubic and intermediate phase stability.

**PACS.** 61.30.-v Liquid crystals – 64.70.-p Specific phase transitions – 83.70.-f Material form

## 1 Introduction

The importance of crystalline bicontinuous morphologies in condensed atomic and molecular systems is now broadly recognized [1,2]. Examples can be found in covalent atomic crystals, such as zeolites [2]; lyotropic liquid crystals [3–5], including lipid-water biochemical systems [6,7] and synthetic surfactant systems [8]; mesoporous inorganic materials synthesized in the presence of amphiphiles [9–12]; in thermotropic liquid crystals [13,14]; block copolymer melts [15,16]; ultrastructured biomimetic skeletons of sea-urchins [17], and cell membranes [18], apparently *in vivo*. Related disordered bicontinuous morphologies are also prevalent in condensed systems, such as “sponge” mesophases in lyotropic systems [19–21], condensed mesoporous inorganics [22], and late-stage spinodals [23]. Given the wide occurrence of these morphologies, the need for a fundamental understanding of the range of competing structures, and their attendant relative stabilities, is evident.

The subtlety of amphiphile aggregation behaviour, revealed through structural studies of soft materials, continually challenges the existing framework of physical theories for self-assembly. The classical DLVO theory [24] of colloidal interactions requires a reformulation for microstructured fluids which accounts for the significant thermal fluctuations of the interfaces. The basis for this renormalization is the bending Hamiltonian of Helfrich [25]. The intrinsic free-energy of an interfacial

state is expressed as an expansion in the geometrical invariants of the dividing surface. For a symmetric, spontaneously flat, bilayer the bending energy per unit midsurface area is then

$$g = 2k_c H^2 + \bar{k}_c K + \dots \quad (1)$$

in which  $H = (c_1 + c_2)/2$  and  $K = c_1 c_2$  are the mean and Gaussian curvatures, *i.e.* the first and second invariants in the local principal curvatures  $c_i$ . Moreover, if the bare repulsion of ionic surfactant bilayers across the solvent domains is sufficiently short ranged, then its free energy contribution for an arbitrary (weakly curved) interfacial configuration can be incorporated consistently into this general prescription, through an additional contribution to the intrinsic bending moduli  $k_c$  and  $\bar{k}_c$  [26]. Within this approximation, the determination of free energies of bilayer systems reduces to the primarily geometrical task of choosing a sufficiently complete set of fluctuation modes for summation. For a lamellar phase, the undulation amplitudes are decomposed into Fourier modes and treated within the harmonic (or a pseudo-harmonic) approximation. In the case of purely steric repulsion, the thermal fluctuations were found to give rise to a long ranged repulsive force [25]. For charged lamellae, the transition from entropy- to energy-dominated repulsion with decreasing ionic strength has been the subject of detailed investigations [27].

In bicontinuous cubic ( $V_2$ ) and sponge phases the bilayer partitions the solvent into a pair of interwoven multiply-connected tunnel systems. The Helfrich Hamiltonian implies that these structures, on average, be based

<sup>a</sup> e-mail: Andrew.Fogden@fkem1.lu.se

upon midsurfaces which, as for the lamellar sheets, possess zero mean-curvature, but now bear negative Gaussian curvature. Owing to the difficulty of geometrically formulating an ensemble of hyperbolic interfacial configurations, one cannot then aspire to the level of statistical mechanical sophistication attainable for lamellar phases. For idealized disordered sponges some progress has, though, been possible using Gaussian random fields [28].

For cubic phases, the focus of thermodynamic descriptions has rested principally on the zero temperature limit of a (fluid) bilayer mid-surface possessing identically zero mean-curvature throughout, *i.e.* an infinite periodic minimal surface (IPMS). Small angle scattering data collected from  $V_2$  phases have to date [4–8] revealed three predominant symmetries, corresponding to those of the three topologically simplest examples of IPMS, the  $G$  (gyroid),  $D$  (diamond) and  $P$  (primitive) surfaces [29,30]. Although these models have been broadly successful, their neglect of fluctuations gives rise to a ground-state degeneracy (vanishing bulk and shear moduli) in the Helfrich description of cubic phases [31]. This degeneracy can, however, be lifted by introducing higher orders to equation (1), specifically a fourth-order term in  $K^2$ . To construct an ensemble of partitions about the three cubic surfaces, an obvious starting point is their lower symmetry generalizations, namely the rhombohedral and tetragonal IPMS families obtained by distortion along a 3-fold or 4-fold axis, respectively. These special modes could be expected to furnish important contributions to fluctuation entropy, since it is the freedom of such minimality – preserving ( $H = 0$ ) degradations which causes the harmonic degeneracy in the cubics. Our objective in this paper is to explicitly construct these families of cubic distortions and determine their Gaussian curvature variations.

Knowledge of the mathematics of lower symmetry IPMS has developed over the past few years [32–34], but is far from complete. Sadoc and Charvolin provided a topological picture of the simplest pathway linking the  $G$ ,  $D$  and  $P$  surfaces, in which the junctions of their bicontinuous labyrinths are systematically merged [3]. A similar mechanism, also phrased in terms of the labyrinth nets, was recently discussed [35], with the argument that the intermediate states of its cubic transitions would be energetically highly unfavourable due to deviations of the corresponding midsurfaces from minimality. In the present study we demonstrate that these types of pathway can, in fact, be traced using exactly minimal surfaces. Specifically, the union of the rhombohedral and tetragonal deformation families provides direct routes between their three cubic parents. Thus, the relevance of these families, and the variations in Gaussian curvature they bear, extends beyond fluctuations to provide fully developed structural pathways, together with the associated bending-energy barriers.

The unified structural picture which emerges can serve to further elucidate the epitaxial relationships for lyotropic systems exhibiting first-order transitions from the  $G$  to  $D$  and/or  $D$  to  $P$  types of bicontinuous cubic phases in lipid-water and surfactant-water

mixtures [6–8,36]. Even more pertinent are the increasingly frequent observations of lyotropic liquid-crystalline phases which display optically anisotropy. The vast majority of the known examples exhibit either rhombohedral or tetragonal symmetry [6,37]. The resolution of interfacial topology is subtle: these phases have, to date, been presumed to be “mesh” structures (with 2-dimensional channel networks, in contrast to the 3-dimensional networks of bicontinuous phases) [38]. The rhombohedral and tetragonal IPMS families explored here offer competing bicontinuous topologies of the same symmetry classes.

Due to the general geometrical nature of this study, the results bear on the diversity of microstructured systems mentioned above. Detailed consideration of non-cubic bicontinuous and mesh morphologies are equally applicable to these systems. For example, block copolymer melts exhibit liquid-crystalline mesophases analogous both in type and sequence to the lyotropics. Even with transmission electron microscopy, it is often difficult to clearly distinguish bicontinuous and mesh phases since image textures change drastically with the sample section [39]. The families which link the simplest isotropic IPMS are likely to offer a useful aid towards recognition of complex microdomain morphologies, and may help to resolve controversies over  $G$  and  $D$  cubic structures in copolymer systems [40].

## 2 Distortions of the D, G and P surfaces

In Figure 1 we show the translational unit cells of the  $D$ ,  $G$  and  $P$  surfaces, with space-groups  $Pn\bar{3}m$ ,  $Ia\bar{3}d$  and  $Im\bar{3}m$ . All three surfaces are “balanced” since they bear embedded symmetry elements, *i.e.*  $\bar{1}$  (inversion) points together with 2-fold lines for  $D$  and  $P$ , which interchange the two sides of the surface and the two skeletal labyrinths partitioned by it. Thus the 4-connected labyrinths of the  $D$  surface are related by translation, as are the 6-connected pair for the  $P$  surface, while the 3-connected networks for  $G$  are enantiomorphic. The overall cell topology is indexed by the Euler characteristic  $\chi$ , which equals  $-2$ ,  $-8$  and  $-4$  per the units of  $D$ ,  $G$  and  $P$  in Figure 1. If the IPMS are used in an unbalanced context – *e.g.* the labyrinths are “colored” to be symmetrically distinct – then these space-groups must be replaced by their black-white subgroups, so the  $D$  unit cell in Figure 1a is doubled in all three directions to allow a full rotation of the surface normal  $\hat{n}$  [41].

The balanced cells in Figure 1 can be generated *via* their internal symmetries from the 3-sided asymmetric patches shown there (comprising fractions  $1/48$ ,  $1/192$  and  $1/96$ , respectively, of the cell). The Gauss maps of the three patches, given by the image regions traced by  $\hat{n}$  onto the unit sphere, are identical, bounded by a triangle of great circle arcs meeting at angles  $\pi/3$ ,  $\pi/4$  and  $\pi/2$  and covering  $1/48$  of the sphere. The three IPMS are thus related by the Bonnet transformation [30]; such patches can be bent continuously into each other, preserving curvilinear line lengths, areas and curvatures. Such Bonnet-related isometric IPMS are thus locally indistinguishable

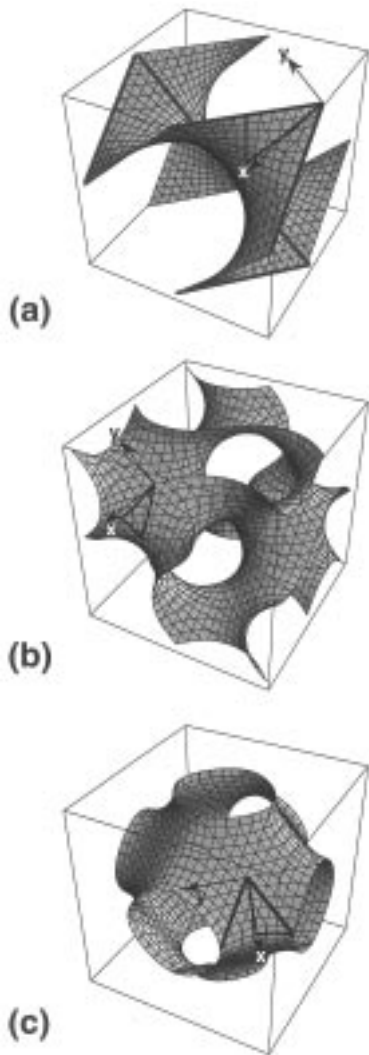


**Fig. 1.** The unit cubes of the (a)  $D$ , (b)  $G$ , and (c)  $P$ , surfaces. The common  $z$ -axis, not shown, is perpendicular to  $(x, y)$ .

in a 2-dimensional sense, with their global embeddings in 3-dimensional space distinguished solely by their association variable, the Bonnet angle. The  $D$  surface patch is bounded by two lines (embedded 2-fold axes) and one mirror plane curve, while the opposite is true of the  $P$  patch, so they are related by a quarter cycle and termed an “adjoint” pair.

For the continuum of bent states intermediate to  $D$  and  $P$  the patch boundary segments are neither straight nor planar, yet the point-group symmetries ascribed to their vertices ( $\bar{3}$ ,  $\bar{4}$  and 2 about the respective  $\hat{n}$ ) are preserved. The  $G$  surface is the unique member for which these elements lock into a crystallographic scheme ( $Ia\bar{3}d$ ) completely free from self-intersections [30]. For all other intermediates, continuation of the patch *via* these symmetries creates intersections which, in the generic case, eventually densely fill 3-dimensional space. Thus a physical, self-avoiding transformation route  $D \rightarrow G \rightarrow P$  using the Bonnet transformation alone would entail an orchestrated process of cutting, bending and gluing patches.

As an illustration, the  $D$  and  $P$  surfaces can both be generated by repeated 2-fold rotation of an element comprising a catenoidal neck spanning a coaxial pair of equilateral triangular frames screwed by  $\pi/3$  (parts of these frames are highlighted in Figs. 1a and 1c). Such catenoidal pieces do not remain topologically intact throughout the Bonnet bend; their frames are cut and resealed as helices winding around the 3-screw axis tunnels in the gyroid.

All three of the surfaces (indeed any IPMS) can be continuously deformed by crystallographic degradations which preserve their minimality and topology. The cubics can be systematically degraded to liberate one-variable families of rhombohedral or tetragonal variants, two-variable orthorhombics, and so on. The rhombohedral distortions of the  $D$  and  $P$  surfaces are obtained by pulling along the  $z$ -axis in Figures 1a and 1c (in the  $[\bar{1}11]$  direction), stretching the screwed triangular catenoidal units shown there. This operation yields a single unifying IPMS family, denoted  $rPD$  and of space-group  $R\bar{3}m$ , in which the  $D$  is transformed to the  $P$  by halving the separation distance between the triangle frames [30, 34, 41, 42]. So by introducing a crystalline anisotropy, these two end states of the (isotropic and isometric) Bonnet transformation can be accessed continuously without slicing or fusing.

Rhombohedral distortions of the gyroid have been investigated only relatively recently, owing to the challenge of visualizing such surfaces. Unlike the straight line frames maintained in the  $rPD$  family, the  $G$  surface contains no fixed boundaries upon which to base the distortion. Nevertheless, its rhombohedral “stretching” freedom (along this same  $z$ -axis direction in Fig. 1b) is again guaranteed by general principles, giving rise to a one-variable family christened  $rG$ , of space-group  $R\bar{3}c$  [43]. In Figure 2 we show a different piece of the cubic  $G$  surface – one that is larger than the patch in Figure 1b; the normal  $\hat{n}$  now traces 1/6 of the unit sphere. This piece is oriented with respect to the coordinates  $(x, y, z)$  in Figure 1b and is viewed both obliquely (Fig. 2a) and in plan view (Fig. 2b, for a hexagonal cell description). In both views only the symmetry elements of  $Ia\bar{3}d$  which remain in its subgroup  $R\bar{3}c$  are included, so the scheme represents a general  $rG$  member. The boundary point  $A$  remains a  $\bar{3}$  site,  $B$  and  $E$  are degraded to  $\bar{1}$ , while 2-fold axes pass through points  $C$  and  $D$  along their  $\hat{n}$  directions indicated there. For later comparison, Figure 2b also displays the shadow of a  $rPD$  surface piece spanning the screwed triangular frames (in gray), with respect to the  $(x, y, z)$  orientation in Figures 1a and 1c.

In the next section (and Appendix A) we shall analyse in detail these rhombohedral distortions of  $D$ ,  $G$  and  $P$ . Previously, one of the authors numerically constructed some examples of  $rG$  surfaces [43], and in particular, demonstrated that the  $HG$  surface discovered in an earlier study [44] is a member of this one-variable family. These preliminary studies are extended here to a full analytic investigation of the  $rG$  family using complete elliptic integrals. In doing so, certain errors in the previous work are corrected. Importantly, it will be established that the rhombohedral stretching of the  $G$  surface ultimately

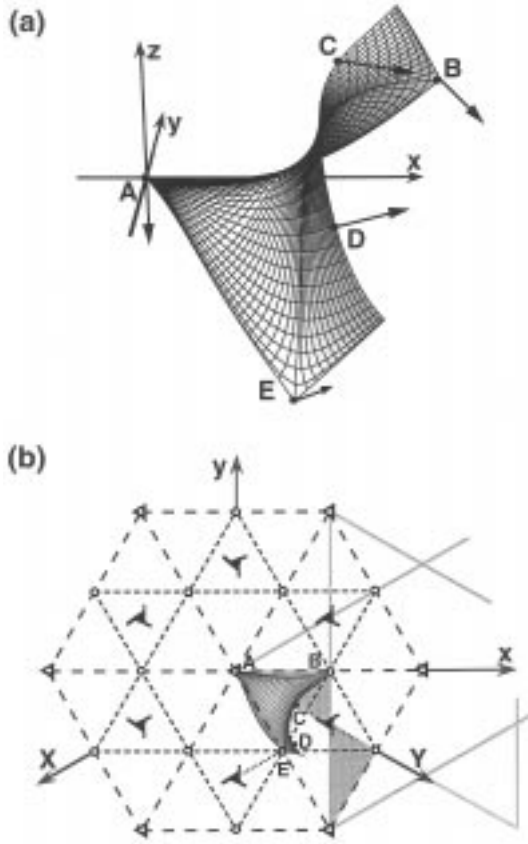


**Fig. 2.** A piece of the  $G$  surface in its rhombohedral aspect, showing (a) the trace of its boundary normal vectors, and (b) the symmetry scheme from above.

restores a member of the  $rPD$  family linking  $P$  to  $D$ . The coupling of these two families gives a “ $rGPD$ ” unification, allowing continuous minimal-surface access between all three cubics. This offers an interesting alternative to the Bonnet transformation route. All quantitative features of the  $rGPD$  surfaces, including cell axis lengths, areas and their Gaussian curvature moments, will be presented.

Systematic removal of the 3-fold symmetry axes of a cubic minimal surface leads to a one-variable IPMS family of tetragonal degradations. For the three simplest cubics, the elliptic integral derivation of their tetragonal generalizations proceeds in direct analogy with the above, and the results are briefly summarized in a following section (and Appendix B). The degradations  $tD$  and  $tP$  were the first IPMS families to be discovered [29,32–34,42]. In contrast to  $rPD$ , these two tetragonal families do not merge, since the cubic  $D$  and  $P$  cannot be simply related by stretching along a 4-folds axis (the  $P$ -generating unit of a catenoidal neck spanning two overlain square frames, in Fig. 1c, is not present in the  $D$ ). Aside from this distinction, the tetragonally distorted gyroids  $tG$  play the same role as their rhombohedral counterparts. The degradation is found to ultimately lead to a  $tD$  surface, thus providing an alternative route for direct structural transformation between the cubic  $G$  and  $D$ .

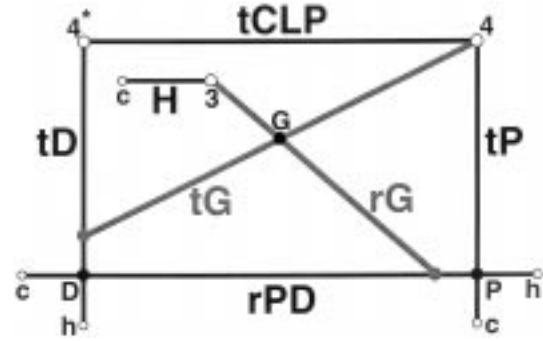


**Fig. 3.** Layout of the three cubic IPMS and the pathways of their 3- and 4-fold generalizations and relatives. The diagonal paths through  $G$  are the main focus of this study. The terminals (open circles) of the families are labeled 3 and 4, representing saddle towers of this symmetry (\* denotes the adjoint), or  $h$  and  $c$  to indicate helicoid and catenoid.

The interrelations covered in this study are represented diagrammatically in Figure 3. We include the hexagonal  $H$  and tetragonal  $tCLP$  families [29,30,32–34] to complete the set of (balanced) IPMS sharing the lowest attainable genus ( $g \equiv 1 - \chi/2 = 3$  per black-white primitive unit cell) and possessing at least 3- or 4-fold symmetry. Although these extra two families are closely related in parametrization, they are topologically distinct within this class and cannot be transformed to any of the three cubics without first taking the in-plane periodicity to infinity (creating a 3- and 4-fold “saddle tower” [45] or its adjoint). The Gaussian curvature distributions of the  $H$  and  $tCLP$  families are less homogeneous than those of the cubics, thus providing a useful comparison with the growing heterogeneity in the cubic distortions.

### 3 Analysis of the rhombohedral surfaces

The Gauss map of the piece of a generic  $rG$  surface represented in Figure 2 is the shaded  $2\pi/3$  sector displayed in Figure 4 in stereographic projection (*i.e.*  $\hat{n}$  taken on the unit sphere is then projected from the north pole onto the equatorial plane, regarded as the complex  $\omega$ -plane). In particular, the  $\bar{1}$  surface site  $B$  is imaged to some point  $\omega = \omega_0 = r_0 \exp(i\phi_0)$  at which the dihedral angle is doubled (from  $\pi/2$  to  $\pi$ ), illustrating a general property of embedded inversion centers (also at  $E$  and  $A$ ). The 3-fold surface symmetry about  $A$ , and the 2-folds about  $C$  and  $D$ , are manifested as the same rotational symmetries on the sphere. So continuation of the surface piece gives multiple copies of a 6-tiling of the sphere and the full group  $\{\omega_n\}$  of 6 rotated images of  $\omega_0$  marked in Figure 4.

The embedding of all minimal surfaces in 3-dimensional Euclidean space can be parametrized by reconstructing the surface from its image in the  $\omega$ -plane

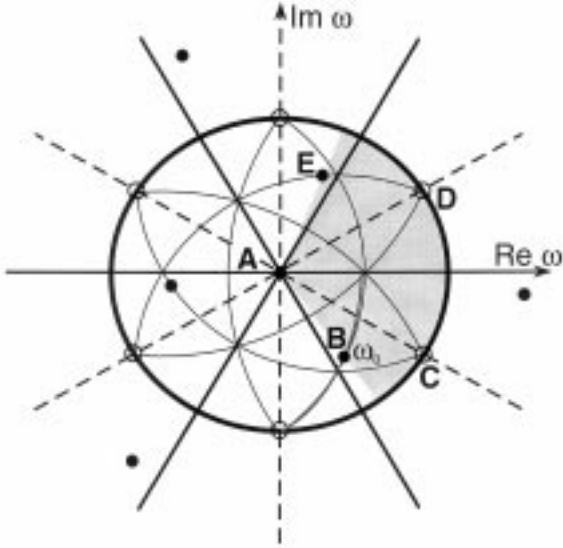


**Fig. 4.** The analytic structure of the  $rG$  family in its parameter space (see the text).

via the Weierstrass representation

$$(x(\omega), y(\omega), z(\omega)) = \text{Re} \left\{ e^{i\theta} \int_0^\omega d\omega' (1 - \omega'^2, i(1 + \omega'^2), 2\omega') \right. \\ \left. \times R(\omega', \omega_n) \right\}. \quad (2)$$

At any point  $\omega = u + i\nu$  the surface metric is thus simply defined as

$$dS = dud\nu(1 + |\omega|^2)^2 |R(\omega, \omega_n)|^2 \quad (3a)$$

and the Gaussian curvature is

$$K = -4(1 + |\omega|^2)^{-4} |R(\omega, \omega_n)|^{-2}. \quad (3b)$$

The choice of the complex analytic function  $R$  is dictated by the symmetry and topology of the IPMS [34], and the general form for the reconstruction of  $rG$  is particularly simple. It must possess first-order branch points at the eight  $\hat{n}$  corresponding to  $\bar{1}$  sites ( $\omega = 0, \infty$ , and the six  $\omega_n$ ), and is given by

$$R(\omega, \omega_n) = [\omega(\omega^3 - \omega_n^3)(\omega^3 + \omega_n^{-3})]^{-1/2}. \quad (4)$$

The Bonnet associates are then obtained by varying the (real) angle  $\theta$  in equation (2), which has no effect on the local areas and curvatures in equation (3). The layout in Figure 4, and hence the choice in equation (4), is not restricted to the  $rG$  family alone, but also contains the  $rPD$  family and the hexagonal  $H$  surfaces [34]. Combining equations (2) and (4), the contour integrals for the surface coordinates are expressible in terms of elliptic integrals – the necessary mathematical manipulations are given in Appendix A as equations (A.1–A.3). These coordinates contain the three, as yet free, variables  $\phi_0$ ,  $r_0$  and  $\theta$ .

For the three cubic surfaces, the 4-folds symmetries give to the Gauss map the geodesic tiling substructure shown with faint lines in Figure 4 (each tile is the image of one small patch in Fig. 1). The eight  $\hat{n}$  entering into equation (4) now run along cube body diagonals so  $\phi_0 = -\pi/3$  and  $r_0 = 1/\sqrt{2}$  in our orientation, which is, for convenience, rotated by  $-\pi/3$  relative to that used in earlier accounts [43]. It only remains to specify the degree of Bonnet bend  $\theta$  (which is now shifted by  $-\pi/2$  as a consequence of this reorientation). The  $D$  and  $P$  surfaces then correspond to the special values  $\theta = -\pi/2$  and  $0$ , respectively, thus ascribing to this adjoint pair the mirror and embedded 2-fold symmetries. The  $G$  surface is locked into the space-group  $Ia\bar{3}d$  by forcing the inversion center  $B$ , with image  $\omega_0$ , to satisfy  $y(\omega_0) = 0$  (see Fig. 2b). The 4-fold (not shown there) then ensure that all other point-group symmetries simultaneously lock in. This constraint on the bend then implies [30]

$$\theta = -\arctan[K'(1/2)/K(1/2)] = -90^\circ + 38.015^\circ. \quad (5)$$

(Note that this  $K$ , the complete elliptic integral [46] used throughout the appendices, is not to be confused with the Gaussian curvature in Eq. (3b).)

The one-variable families of rhombohedral distortions from these cubics correspond to a single residual degree of freedom in the Gauss map, resulting from a pair of constraints on  $\phi_0$ ,  $r_0$  and  $\theta$ . The  $rPD$  family, generalizing the  $P$  and  $D$  surfaces, is obtained by fixing  $\theta = -\pi/2$  or  $0$  and simply sliding the six points  $\omega_n$  along the six (solid) radial lines in Figure 4 [34]. These two symmetry requirements ensure that the embedded 2-fold axes framing the catenoidal units in Figures 1a and 1c are maintained, together with their subdividing mirror planes. For our choice of coordinate orientation we use the convention  $\theta = -\pi/2$  and  $\phi_0 = 0$  for  $rPD$ , allowing  $\omega_0$  to run along the entire positive real axis ( $0 < r_0 < \infty$ ), passing through the cubic  $P$  and  $D$  at  $r_0 = 1/\sqrt{2}$  and  $\sqrt{2}$ , respectively. Since the  $rPD$  surfaces can be obtained as a special case of the general constructs for  $rG$ , we begin our analysis with the latter family.

For the  $rG$  family the prerequisite point-group symmetries are guaranteed by the form of equations (2, 4); instead it is their relative positions in the space-group which must be maintained through a pair of constraints. As shown in Figure 2b with respect to the crystallographic cell coordinates  $(X, Y, Z)$ , the points  $A, B, C, D$  and  $E$  must mutually lock into the sites, or lines,  $(0, 0, 0)$ ,  $(-1/6, 1/6, 1/6)$ ,  $(0, Y_C, 1/4)$ ,  $(X_D, 1/3, 1/12)$ , and  $(1/6, 1/3, -1/6)$ . Our Cartesian coordinates are given by

$$X = -\frac{1}{\sqrt{3}} \frac{x}{a} - \frac{y}{a}, \quad Y = \frac{1}{\sqrt{3}} \frac{x}{a} - \frac{y}{a}, \quad Z = \frac{z}{c} \quad (6)$$

so  $(x, y, z)(\omega_0) = (a/(2\sqrt{3}), 0, c/6)$  and we must impose  $y(\omega_0) = 0$  as for the cubic  $G$  surface mentioned above. Due to the 4-fold degradation of  $Ia\bar{3}d$ , a second condition is necessary, and moreover sufficient, for lock-in to the rhombohedral space-group  $R\bar{3}c$ . The  $\bar{3}$  site with image  $\omega = \infty$  has position  $(x, y, z)(\infty) = (0, 0, c/2)$  and thus

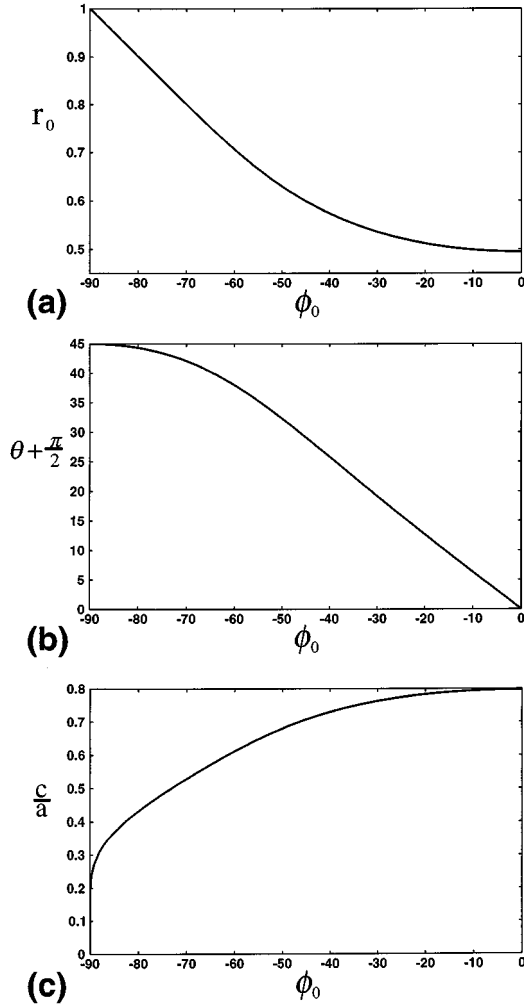


**Fig. 5.** The (a) branch-point magnitude  $r_0$ , (b) Bonnet angle  $\theta$  (in degrees), and (c) ratio of vertical to horizontal periods  $c/a$ , corresponding to each member, *i.e.*  $\phi_0$  value (in degrees), of the  $rG$  family.

we demand that  $z(\omega_0) - z(\infty)/3 = 0$ . In equations (A.4, A.5) we formulate these constraints on  $rG$  using the general elliptic integral representation. This provides a single transcendental equation relating  $r_0$  and  $\phi_0$ , with the Bonnet association angle  $\theta$  and the hexagonal cell lengths  $a$  and  $c$  for  $R\bar{3}c$  then given explicitly in terms of these two. We choose the argument  $\phi_0$  as the independent variable for the  $rG$  family, swinging through the range  $-\pi/2 < \phi_0 < 0$ . The trajectory  $r_0(\phi_0)$  of the solutions in the complex plane is as sketched in dark gray in Figure 4.

The exact numerical solutions for  $r_0$ ,  $\theta$  and the axis ratio  $c/a$  are plotted against  $\phi_0$  in Figures 5a, 5b (which is shifted up by  $\pi/2$  for simplicity) and 5c, respectively. Recall that the cubic  $G$  surface is given by  $\phi_0 = -\pi/3$ ,  $r_0 = 1/\sqrt{2}$ , with the  $\theta$  value in equation (5), and  $c/a = \sqrt{3}/2$ . As  $\phi_0$  decreases to approach  $-\pi/2$ ,  $r_0$  increases to unity and the  $\{\omega_n\}$  merge pairwise on the equator in Figure 4. This creates a degenerate surface with

infinite ends, *i.e.*  $a \rightarrow \infty$  at finite  $c$ ; the ratio  $c/a$  decreases sharply to zero in the vicinity of this endpoint. The limiting surface (with  $\theta = -\pi/4$ ) is the 3-fold saddle tower of Karcher [45]. On the other hand, as  $\phi_0$  increases from the cubic  $G$  case to reach  $-\pi/6$ , the  $\{\omega_n\}$  lie on rays dotted in Figure 4 and are mirror related in the equatorial plane. The surface is then the special, intersection-free member of the Bonnet transformations of the hexagonal  $H$  family, called  $HG$ , with  $r_0 = 0.53607$  and  $\theta = -90^\circ + 19.2098^\circ$  (agreeing with previous studies [43,44]). This additional symmetry in the Gauss map is not evidenced in Euclidean space, so the  $HG$  surface displays the common  $R\bar{3}c$  symmetry, with  $c/a = 0.76327$ . As  $\phi_0$  increases further and tends to zero,  $\theta$  approaches  $-\pi/2$  and  $r_0 \rightarrow 0.49472$ , with  $c/a = 0.79746$ . This  $rG$  endpoint is thus a non-degenerate member of the  $rPD$  family (correcting an earlier conclusion [43]). So the two families join at this common surface, creating the  $rGPD$  union, which provides a *continuous* pathway of IPMS linking all three simplest cubic surfaces.

Figure 6 is a scan of the  $rG$  family, displaying the (intersection-free) IPMS corresponding to four  $\phi_0$  values.

Each surface unit shows the screw-axis repeat of three monkey saddles (*i.e.* 18 of the pieces in Fig. 2 for the cubic gyroid in Fig. 6c), again in both oblique and plan views, with the perspectives and orientations fixed throughout. In passing from Figure 6c to 6d, the  $G$  surface flattens to approach infinite saddle towers; the curves connecting the saddle centers gradually straighten and lengthen so the helix becomes more planar. On passing back from the  $G$  to  $HG$  surface in Figure 6b, these trends continue – the tunnel down the screw axis is now significantly tighter. Proceeding further to Figure 6a, the tunnel eventually vanishes completely due to the formation of embedded 2-fold axes (crossed triangular frames) which exchange the mirror plane curves connecting the saddle centers, and thus the  $rPD$  family is reached.

The surface area  $S$  of an IPMS cell is commonly expressed *via* the dimensionless ratio  $\sigma = S/V^{2/3}$ , where  $V$  is the cell volume. However, the value of this quantity for a given IPMS is dependent upon the choice of cell. It is more convenient to use the so-called homogeneity index  $\mathcal{H}$  which divides  $\sigma^{3/2}$  by  $[-2\pi\chi]^{1/2} = [\int(-K)dS]^{1/2}$ , and is thus both dimensionless and intensive. Furthermore,  $\mathcal{H}$  takes the value of  $3/4$  for a hypothetical minimal surface with uniform  $K$ , so its deviation from this “ideality” can give some measure of the inhomogeneity in the Gaussian curvature distribution [5]. The surface area  $S_p$  of the smallest representative piece of  $rG$ , such as that in Figure 2, is directly obtained from equation (3a) and expressed *via* complete elliptic integrals in equations (A.6, A.7). In terms of this and the unit cell dimensions  $a$  and  $c$  already determined, the homogeneity index for the  $rG$  family is

$$\mathcal{H} = \frac{S^{3/2}}{[-2\pi\chi]^{1/2}V} = 36\sqrt{\frac{2}{\pi}} \frac{S_p^{3/2}}{a^2c}. \quad (7)$$

More direct measures of the inhomogeneity are given by the surface area averages (denoted  $\langle \rangle$ ) of powers  $q$  of the Gaussian curvatures. We consider the normalized

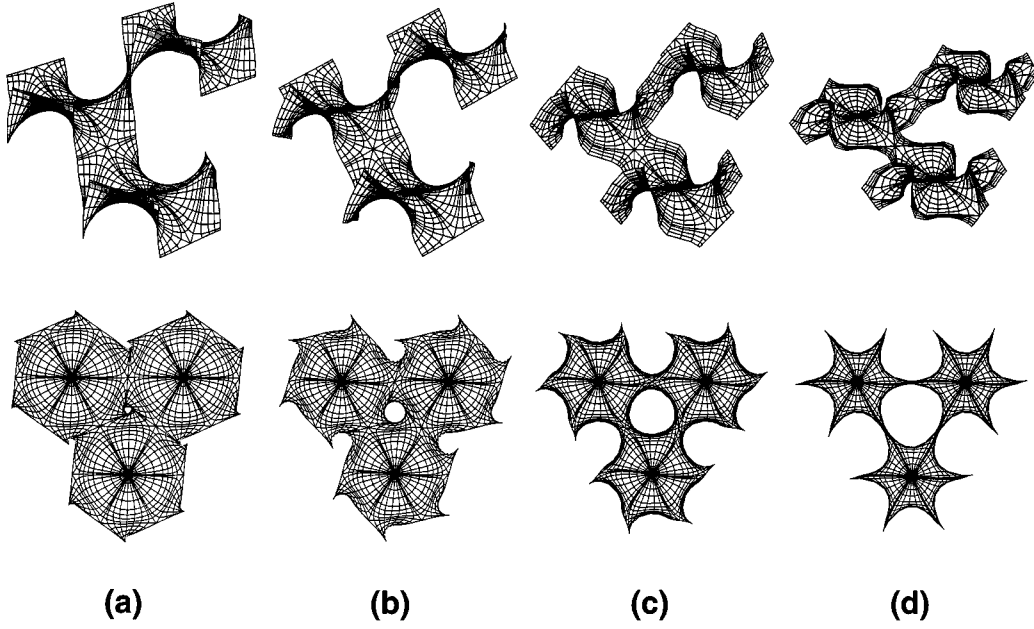


**Fig. 6.** Units of the  $rG$  surfaces corresponding to the  $\phi_0$  values (a)  $-10^\circ$ , (b)  $-30^\circ$ , (c)  $-60^\circ$  and (d)  $-80^\circ$ , each shown in both perspective and plan views.

quantities

$$\mu_q \equiv \frac{\langle |K|^q \rangle}{\langle |K| \rangle^q} = \left( \frac{3}{2\pi} \right)^q S_p^{q-1} \int (-K)^q dS_p \quad (8)$$

over these same surface pieces, again making use of the definitions in equation (3).

The indices in equations (7, 8) for the  $rG$  surfaces are plotted, *versus*  $\phi_0$ , in Figures 7a and 7b. In the latter we consider powers  $q = 1/2, 3/2, 2, 5/2$  and  $3$  ( $\mu_q$  is unity for  $q = 0$  or  $1$ ). For the cubic gyroid  $\mathcal{H} = 0.766668$  [30] and represents the absolute maximum over the family. As  $\phi_0$  decreases from  $-\pi/3$ ,  $\mathcal{H}$  descends increasingly steeply and approaches zero vertically (not included in the range of the figure) at the saddle tower endpoint. On the other side,  $\mathcal{H}$  decreases slowly, through a value of  $0.755043$  at the  $HG$  surface, and reaches a local minimum of  $0.748837$  at the  $rPD$  surface. In Figure 7b the plots of the Gaussian curvature moments  $\mu_q$  are all of the same shape for  $q > 1$ , with their absolute minima fixed at the cubic  $G$  (values of  $1.0891, 1.2188, 1.3896$  and  $1.6068$  for  $q = 3/2, 2, 5/2$  and  $3$ ), rising to infinity as  $\phi_0$  approaches  $-\pi/2$  and rising to local maxima at the opposite end (with corresponding values  $1.1638, 1.4376, 1.8543$  and  $2.4688$ ). For powers  $0 < q < 1$  the situation is reversed;  $\mu_{1/2}$  has similar characteristics to  $\mathcal{H}$  in Figure 7a, with maximum value of  $0.95903$  at the  $G$  surface and a local minimum of  $0.93544$  at the  $rPD$  cross-over.

We complete the analysis of the  $rGPD$  union by briefly summarizing the results for the  $rPD$  family, in order to understand the  $rG$  endpoint surface in the context of this continuum. Recall that the  $rPD$  surfaces are the special case of equations (A.1–A.7) in which the crystallographic constraints reduce to  $\theta = -\pi/2$  and  $\phi_0 = 0$ . The cell dimensions  $a$  and  $c$  are then expressed simply in terms

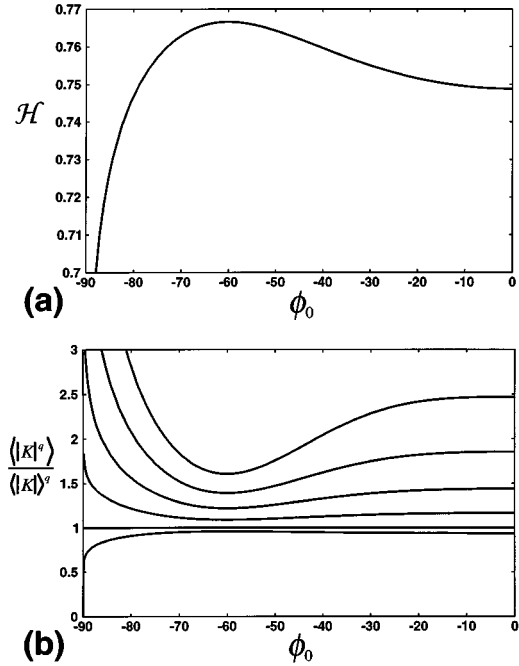


**Fig. 7.** Plots of the (a) homogeneity index, and (b) averaged Gaussian-curvature taken to powers  $q = 1/2, 1$  (straight line),  $3/2, 2, 5/2$  and  $3$  in ascending order, across the  $rG$  family.

of the free variable  $r_0$  in equations (A.8–A.10). Since the formalism was constructed for  $rG$ , this height  $c$  refers to the space-group  $R\bar{3}c$ . To avoid ambiguity we shall adhere to this definition, bearing in mind that the  $Z$  values of the  $R\bar{3}c$  hexagonal cell (see Fig. 2b and Eq. (6)) must be doubled, and thus the  $c$  value halved, for the true  $rPD$

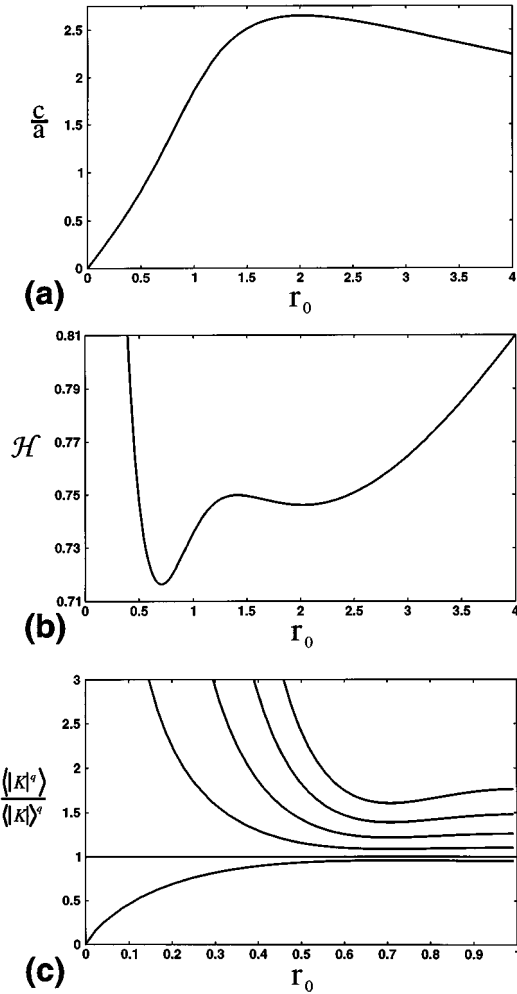


**Fig. 8.** The (a) ratio  $c/a$ , doubled for the space-group  $R\bar{3}c$ , (b) homogeneity index, and (c) averaged Gaussian-curvature raised to powers  $q = 1/2, 1$  (straight line),  $3/2, 2, 5/2$  and  $3$  in ascending order, corresponding to each member, *i.e.*  $r_0$  value, of the  $rPD$  family.

symmetry  $R\bar{3}m$ . Figure 8 displays the plots of the hexagonal axis ratio and the two types of homogeneity measure,  $\mathcal{H}$  and  $\mu_q$ , over the  $rPD$  family as a function of  $r_0$ . The latter two indices use the same definitions as in equations (7, 8) for  $rG$  (the surface area  $S_p$  now reduces by symmetry to Eq. (A.11)), with the length  $c$  again pertaining to  $R\bar{3}c$ , not  $R\bar{3}m$ . Figure 9 then shows a scan of six of these  $rPD$  surfaces.

In contrast to Figure 5c, the  $c/a$  curve in Figure 8a has the humped shape characteristic for stretching of a ring-like minimal surface unit [42], decreasing to zero at the endpoints  $r_0 \rightarrow 0$  (helicoid) and  $r_0 \rightarrow \infty$  (catenoid), although the plot only extends to  $r_0 = 4$ . Each ratio corresponds to a pair of  $r_0$  values and thus two distinct  $rPD$  surfaces. At  $r_0 = 0.49472$  the ratio is  $0.79746$  as for the endpoint of Figure 5c. It then increases through values of  $\sqrt{3/2}$  and  $2\sqrt{3/2}$  at the cubic  $P$  and  $D$  surfaces ( $r_0 = 1/\sqrt{2}$  and  $\sqrt{2}$ , respectively). The maximum value is  $2.64882$  and occurs at  $r_0 = 2.02134 = 1/0.49472$ , so the

$rPD$  surface at maximum stretch is adjoint ( $\Delta\theta = \pi/2$ ) to that which is shared with the  $rG$  family. Each of the  $rPD$  pieces in Figures 9a–9f is generated from the same infinite wedge  $0 \leq \arg(\omega) \leq \pi/3$  of the complex plane in Figure 4. Thus they correspond to the pair of triangles shaded in Figure 2b, internally related by the perpendicular 2-fold axis (along the  $\hat{n}$  direction  $D$  in Figs. 2 and 4), and comprising  $1/6$  of the ring-like unit spanning the crossed triangles. The six surfaces group as three adjoint pairs: (a) and (f), (b) and (e), (c) and (d). On decreasing  $r_0$ , the  $rG$  endpoint in Figure 9b (compare with Fig. 6a) is compressed to Figure 9a and approaches the helicoidal limit in which the locus of the horizontal normal vectors straightens to a vertical line. As  $r_0$  increases, (b) is stretched to give the  $P$  and  $D$  surfaces in (c) and (d); note that for  $r_0$  greater than unity these equatorial  $\hat{n}$  switch to run around the neck. The  $rPD$  surface at full extension is displayed in (e). Further increase in  $r_0$  causes a compression of the surface in which the band of equatorial  $\hat{n}$  flattens, in (f), to approach a catenoid.

The homogeneity index is plotted over the range  $0 < r_0 < 4$ , for values less than  $0.81$ , in Figure 8b. It rises without bound at either endpoint and agrees with the established values  $\mathcal{H} = 0.748837, 0.716346$  and  $0.749844$  at the  $rG$  endpoint (Fig. 7a), the  $P$  and the  $D$  [30] surfaces, respectively. Moreover, these latter two cubics represent the global minimum and a local maximum within this  $rPD$  family. The extra local minimum value is  $0.746063$  and occurs at  $r_0 = 2.02134$ , which corresponds to the maximum of the  $c/a$  ratio in Figure 8a. For the Gaussian curvature moments  $\mu_q$ , equation (8) is independent of Bonnet angle and so invariant under inversion of  $r_0$  for any power  $q$ . Hence the plot in Figure 8c is only given over the range  $0 \leq r_0 \leq 1$ . The trends are similar to those for  $rG$ , with all curves displaying a global minimum ( $q > 1$ ) or maximum ( $0 < q < 1$ ) at the cubic  $P$  and  $D$  surfaces. The values of these extrema are identical to those for the cubic  $G$ . At the self-adjoint case ( $r_0 = 1$ ) the symmetry then imposes local extrema (*e.g.* a maximum of  $1.2629$  for  $q = 2$  and a minimum of  $0.95376$  for  $q = 1/2$ ).

Figure 10 summarizes the quantitative global characteristics for the three IPMS families of genus three and 3-fold symmetry, by combining the foregoing results with their analogs for the hexagonal  $H$  surfaces [34]. The dummy variable abscissa has been eliminated from each family (*i.e.*  $\phi_0$  for  $rG$ ,  $r_0$  for  $rPD$  and  $H$ ) to yield direct plots of the variation in the intensive surface/volume ratio  $\mathcal{H}$  (about the value  $0.75$ ) with  $c/a$ , in Figure 10a, and the Gaussian curvature second moment  $\mu_2$  versus  $\mathcal{H}$ , in Figure 10b. We maintain the  $R\bar{3}c$  definition of  $c$  for both  $rG$  and  $rPD$ , to emphasize the topological continuity of the transformation in Figure 10a, while for the  $H$  surfaces the axial ratio refers to their true space-group  $P6_3/mmc$ . For this ring-like family, obtained from  $rPD$  by superposing, rather than crossing, the equilateral triangular frames, the maximum attainable stretch is  $c/a = 0.88400$ . At this limit of extension,  $\mathcal{H}$  has a shallow local minimum of  $0.745793$ , in close proximity to its local maximum of  $0.748806$  at  $c/a = 0.83170$ . The smallest heterogeneity



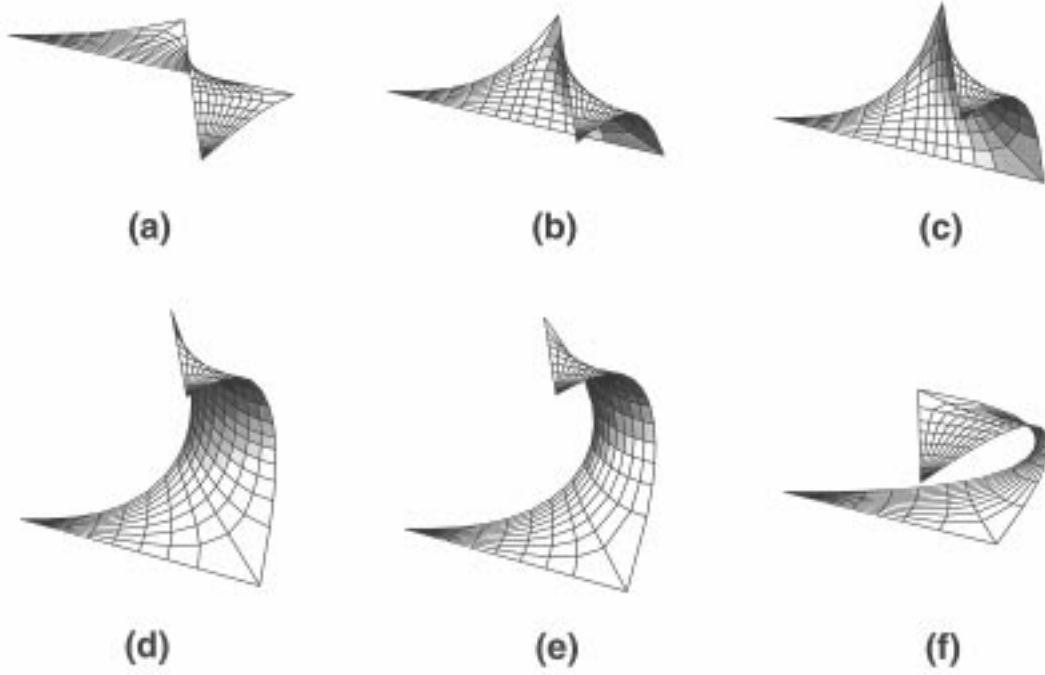


**Fig. 9.** Pieces of the  $rPD$  surfaces at the  $r_0$  values (a) 0.1, (b) 0.49472, (c)  $1/\sqrt{2}$ , (d)  $\sqrt{2}$ , (e)  $1/0.49472$ , and (f) 10.

in curvature for the  $H$  family is  $\mu_2 = 1.3249$ , occurring at  $\mathcal{H} = 0.748125$ . This value is not greatly in excess of the absolute minimum shared by the three cubic IPMS. At the absolute minimum, the slope of the diverging branches of the rhombohedral distortions in Figure 10b is 5.222,  $-12.90$  and  $-17.66$  for  $P$ ,  $D$  and  $G$ , respectively. Although the pair of plots provide immediate access to the surface quantities of use, the convoluted curve shapes (e.g. the  $H$  loop in (b)) warn of the intricacy of geometrical interrelations about  $\mathcal{H} = 0.75$ , in the vicinity of which all three indices display extrema.

#### 4 Analysis of the tetragonal surfaces

The tetragonal distortions of the three cubic IPMS, which retain 4-fold rotational symmetry, follow from application of the same methodology as outlined above; the visualizations and mathematical manipulations are, in fact, now somewhat simpler. Stretching or compression of the cubes in Figure 1 in, say, the vertical direction gives rise to the (a)  $tD$ , (b)  $tG$  and (c)  $tP$  families, with space-groups  $P4_2/nmm$ ,  $I4_1/acd$  and  $I4/mmm$ , respectively. We shall not enter into the details of the parametrizations here. Suffice it to say that the group  $\{\omega_n\}$  of projected inversion-center normals now comprises 8 rotated images of  $\omega_0 = r_0 \exp(i\phi_0)$ , and accordingly, in equation (2) the Weierstrass functional form becomes

$$R(\omega, \omega_n) = [(\omega^4 - \omega_n^4)(\omega^4 - \omega_n^{-4})]^{-1/2} \quad (9)$$

for all three tetragonal IPMS, together with the  $tCLP$  [34]. In Appendix B the pair of crystallographic commensurability constraints for the  $tG$  family, and the resulting surface measures, are phrased in terms of elliptic integrals,

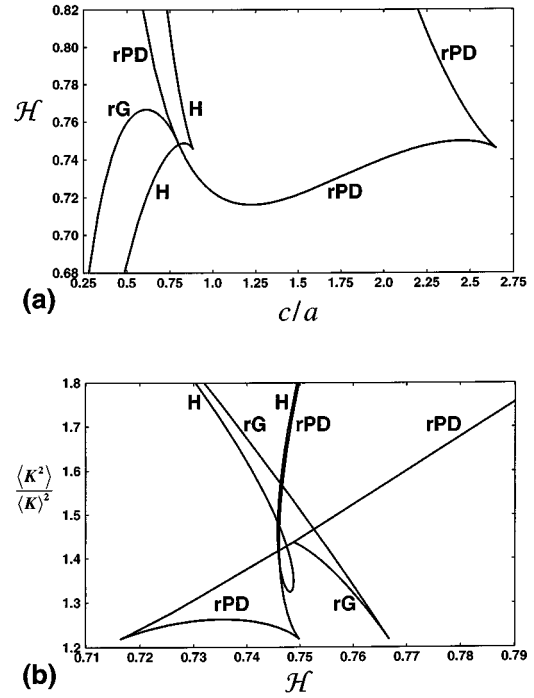


**Fig. 10.** Plots of (a) homogeneity index *versus* cell-axis ratio, and (b) Gaussian-curvature second moment *versus* homogeneity index, for the  $rG$ ,  $rPD$  and  $H$  surfaces.

with the  $tD$  and its adjoint  $tP$  extracted as special cases of the formalism. As for  $rG$ , we take  $\phi_0$ , in the range from  $-\pi/2$  to 0, as the independent variable for the tetragonal gyroids, now with the cubic  $G$  restored at  $\phi_0 = -\pi/4$ ,

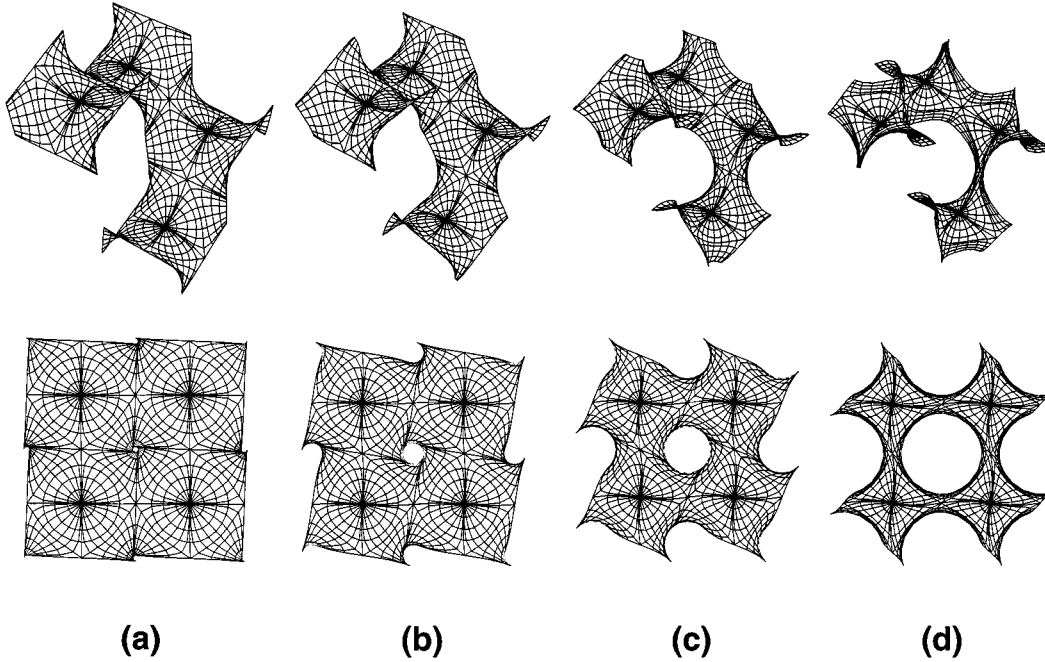


**Fig. 11.** Units of the  $tG$  surfaces for the  $\phi_0$  values (a)  $-5^\circ$ , (b)  $-20^\circ$ , (c)  $-45^\circ$ , and (d)  $-70^\circ$ , in both perspective and plan views.

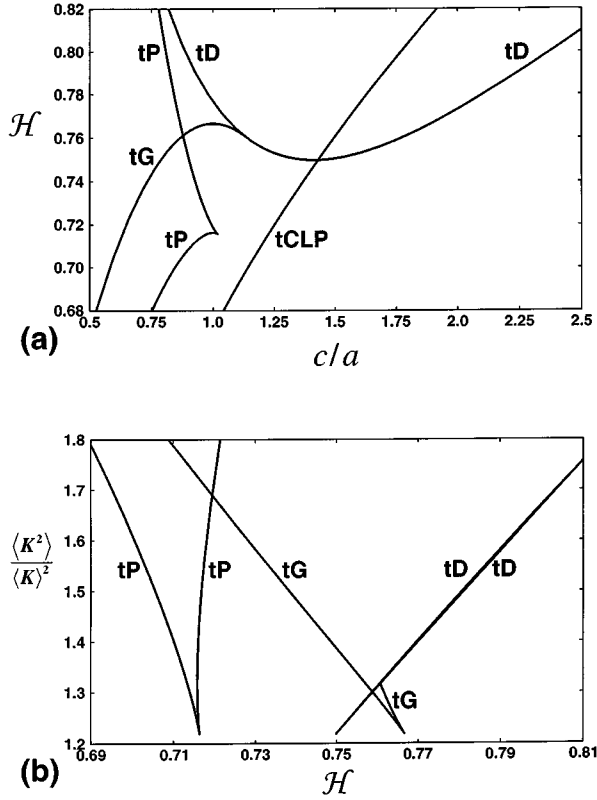
with  $r_0 = (\sqrt{3}-1)/\sqrt{2}$ . However, below we limit our focus to the real-space manifestation of the surfaces.

Figure 11 shows a scan of four representative members of the (intersection-free)  $tG$  family, providing the tetragonal counterpart to Figure 6 – the cubic gyroid is again in part (c). Each of the identical views now contains a repeat unit of four saddles winding around the 4-screw axis. Proceeding from Figures 11c to 11d, the tetragonal axis ratio  $c/a$  decreases from unity to eventually approach zero, losing the  $(x, y)$  periodicity and giving isolated 4-saddle towers. In the opposite direction, the transition from (c) to (b) to (a) with slowly increasing  $c/a$ , results in a rapid tightening of the 4-screw tunnel. Beyond Figure 11a the saddle edges (and the helix they form) become straight lines, thus merging with the  $tD$  family at the particular ratio  $c/a = 1.1315$  (for symmetry  $I4_1/acd$ ), corresponding to  $r_0 = 0.43188$ .

With respect to the homogeneity and Gaussian curvature indices (defined in Eqs. (B.6, B.7)), the cubic gyroid represents an absolute maximum and minimum (for  $q > 1$ ), respectively, over  $tG$ . Away from these extrema,  $\mathcal{H}$  falls to 0.760735 and  $\mu_2$  rises to 1.3165 at the  $tD$  endpoint. The  $tD$  continuum possesses a monotonically increasing  $c/a$  ratio, and its two homogeneity measures both rise without limit from their minima at the cubic  $D$ . On the other hand, the ring-like  $tP$  family is restricted to a maximum extension of  $c/a = 1.0184$  (for  $I4/mmm$ ), only slightly above the cubic  $P$  value of unity [42]. Again, the maximally stretched  $tP$  surface is precisely the adjoint

of the  $tD$  member terminating the  $tG$  family. Moreover, this surface and the cubic  $P$  represent a shallow local minimum and maximum, respectively, of  $\mathcal{H}$  over  $tP$ , with the latter defining the absolute minimum for the Gaussian curvature moments. Thus, comparing the tetragonal and rhombohedral distortions, the  $tG$  transition is qualitatively identical to that for  $rG$  if the  $rPD$  (in Fig. 8) is instead regarded as two separate families, with the half  $0 < r_0 < 1$ , containing the cubic  $P$ , playing the role of the  $tD$  family, and the remainder  $1 < r_0 < \infty$  mimicking  $tP$ .

The behaviour described above is presented in Figure 12, and combined with that for the  $tCLP$  family [34] to provide a unified account of the four IPMS with genus three and 4-fold symmetry, partnering that in Figure 10 for 3-fold symmetry. Again we have retained the  $c/a$  definition for  $tG$  symmetry in plotting the  $tD$  locus in Figure 12a; with respect to its true space-group  $P4_2/nmm$  (used in Appendix B) the values must be reduced by a factor of  $\sqrt{2}$ . For the other two IPMS, the axial ratios are defined in the conventional way, *i.e.*  $P4_2/mcm$  for  $tCLP$ . Since the latter family is not ring-like, but rather owes its name to the Crossed Layers of Parallel tunnels [30], it possesses monotonically varying axial ratios, as well as  $\mathcal{H}$  values. It is absent from Figure 12b since even the most homogeneously curved member, with  $\mu_2 = 1.9614$ , lies above the plotted window (and is thus substantially more heterogeneous than the hexagonal  $H$ ). The gradient of the diverging branches of tetragonal degradations from the absolute minima at the three cubics in Figure 12b are  $-57.12$ ,  $9.067$  and  $-12.10$  for  $P$ ,  $D$  and  $G$ , respectively. For  $tD$ , this slope is maintained over a broad range of  $\mathcal{H}$ , so its two branches are almost overlain.



**Fig. 12.** Plots of (a) homogeneity index *versus* axial ratio, and (b) Gaussian-curvature second moment *versus* homogeneity index, for the *tG*, *tD*, *tP* and *tCLP* surfaces.

## 5 Conclusions

Our analysis completes the elucidation of the simplest class of triply-periodic minimal surfaces, namely those of genus three and possessing 3- or 4-fold symmetry axes. The class comprises the rhombohedral and tetragonal degradations of the cubic *D*, *G* and *P* surfaces, together with the *H* and *tCLP* families. All other intersection-free IPMS sharing this lowest attainable genus are merely reduced symmetry relatives of these families, *e.g.* orthorhombic degradations of the tetragonal and hexagonal space-groups.

Most importantly, this limited class is sufficient for the direct construction of topologically continuous, minimal surface transformations between these three cubic members. As opposed to the Bonnet transformation, for which the ideality of surface isometry necessitates a piecewise orchestration of self-avoidance in Euclidean space, the present mechanism is truly global. Accordingly, it cannot preserve the isometric and isotropic nature of the Bonnet route, *i.e.* maintain the Gaussian curvature variance  $\mu_2$  at its common value 1.2188 for the three cubics (the most homogeneous of all IPMS). However, the costs incurred by increased curvature heterogeneity are relatively slight. In particular, passing with decreasing  $\mathcal{H}$  from the *G* to *D* surfaces along their unified tetragonal families (by increasing the  $c/a$  ratio a factor of  $\sqrt{2}$ ), the “bottleneck” in  $\mu_2$  is 1.3165, occurring at the smooth crossover from *tG* to *tD*

(see Fig. 12). Subsequent passage from *D* to *P* along their rhombohedral *rPD* family, by halving the rhombohedral axis ratio, encounters a  $\mu_2$  bottleneck of only 1.2629, at the self-adjoint member of *rPD* (see Fig. 10). Thus the two-step process, while involving large deformations in unit cell dimensions, introduces less heterogeneity than even the most homogeneously curved *H* surface, and substantially less than any *tCLP* surface. Furthermore, the index  $\mu_2$  increases rapidly with genus (per primitive black-white unit cell), *e.g.* its values for the cubic *I-WP*, *F-RD* and *C(P)* surfaces [30], of genus 4, 6 and 9, respectively, are 1.4838, 1.6156 and 2.8045. Thus it is highly probable that all other conceivable IPMS will exceed the heterogeneity cost of this global transformation  $G \rightarrow D \rightarrow P$ . For these reasons we envision the relevance of the transformation to thermal fluctuations of cubic phases and possible stabilization of anisotropic bicontinuous intermediates.

## Appendix A: Parametrization of the rhombohedral surfaces

The parametrizations of the ordinates  $x$  and  $y$  in equations (2, 4) are expressed as elliptic integrals of the first kind  $F$ , *via* the substitution

$$u = (\omega^{-1} - \omega)/2, \quad (\text{A.1})$$

similarly defining  $u_n$  in terms of  $\omega_n$ . In particular, the modulus  $k$  and prefactor  $G$  of  $F$  are

$$k^2 = \frac{1}{2} \left( 1 - u_n \{ 3 / (4u_n^2 + 1) \}^{1/2} \right),$$

$$G = (3(4u_n^2 + 1))^{-1/4}. \quad (\text{A.2})$$

The  $z$ -ordinate parametrization is simply reduced to elliptic form by changing integration variable to  $\omega^{3/2}$ ; it further serves to apply the Gauss transformation [46], resulting in a new elliptic integral  $F$  with modulus and prefactor

$$k_z = ((\omega_n^6 + 1)^{1/2} + \omega_n^3)^2,$$

$$G_z = \{ -\omega_n^3 / (\omega_n^6 + 1) \}^{1/2} (1 + k_z). \quad (\text{A.3})$$

There are a multitude of equivalent ways of formulating the two closure constraints for the *rG* surface family. We choose here to focus on the position of the  $\bar{1}$  site with  $\omega = \omega_0$ . Imposition of  $y(\omega_0) = 0$  gives the first such constraint, which is used to eliminate the Bonnet angle  $\theta$  in terms of  $\omega_0$ ; the horizontal cell dimension  $a$  is then specified as a function of  $\omega_0$  *via*  $x(\omega_0) = a/(2\sqrt{3})$ :

$$\tan \theta = \text{Re}\{GK(k)\} / \text{Im}\{GK(k)\} \quad (\text{A.4a})$$

$$a = 4|G| \text{Re}\{K(k)K'(k)^*\} / |K(k)|. \quad (\text{A.4b})$$

Here  $k$  and  $G$  are given from equation (A.2) with  $\omega_n = \omega_0$ ,  $K$  and  $K'$  are the complete, and associated complete,

elliptic integrals of the first kind, and the asterisk denotes conjugation. Equivalently, equation (A.4) could be rewritten, replacing  $K$  by  $iK - K'$  throughout, now using  $e^{i\pi/3}\omega_0$  for  $\omega_n$  in equation (A.2). The second closure constraint then forces the height  $z(\omega_0) = c/6$  to be consistent with  $z(\infty) = c/2$ . This gives, in analogy to the pairs above,

$\tan \theta =$

$$\text{Re}\{iG_z(K(k_z) + iK'(k_z))\}/\text{Im}\{iG_z(K(k_z) + iK'(k_z))\} \quad (\text{A.5a})$$

$$c = 4|G_z|\text{Re}\{K(k_z)K'(k_z)^*\}/|K(k_z) + iK'(k_z)| \quad (\text{A.5b})$$

taking  $\omega_n = \omega_0$  in equation (A.3). Due to the branch cut in  $K'(k_z)$ , equation (A.5) can only be used, as written, over the subrange  $\phi_{cut} < \phi_0 < 0$ , where  $\phi_{cut} \approx -1.4527$ . For the remainder,  $-\pi/2 < \phi_0 < \phi_{cut}$ , we must switch the  $\omega_n$  in equation (A.3) to  $e^{i\pi/3}\omega_0$  and also replace the combination  $K + iK'$  in equation (A.5) by  $i3K + 2K'$ .

Equating the independent expressions for  $\tan \theta$  then gives the single constraint on  $\omega_0$ . The resulting equation for  $r_0$  as a function of  $\phi_0$  is of course transcendental, however, its numerical solution is straightforward. The Bonnet angle  $\theta$  and the axis lengths  $a$  and  $c$  are then directly obtained from the above formulae.

The surface area  $S_p$  corresponding to the region  $-\pi/3 \leq \phi \leq \pi/3$ ,  $0 \leq r \leq 1$  in the parameter space  $\omega = r \exp(i\phi)$ , is obtained from equation (3a), which simplifies to the radial integral

$$S_p = \frac{4}{3} \int_0^1 dr (1+r^2)^2 |(r^6 - r_0^6)(r^6 - r_0^{-6})g|^{-1/2} K'(1/g) \quad (\text{A.6})$$

where

$$g = g_1 + (g_1^2 - 1)^{1/2} \quad (\text{A.7a})$$

$$g_1 = \frac{(r^6 - r_0^6)(r^6 - r_0^{-6}) + 2r^6\{(r_0^3 + r_0^{-3})^2 - 4 \sin^2 3\phi_0\}}{|(r^6 - r_0^6)(r^6 - r_0^{-6})|} \quad (\text{A.7b})$$

The  $rPD$  family of surfaces then becomes the special case of equations (A.1–A.7) for which  $\theta = -\pi/2$  and  $\phi_0 = 0$ , with the branch point now free to slide over  $0 < r_0 < \infty$ . The  $rPD$  surface for any such  $r_0$  value is equivalent, aside from a rigid rotation of  $m\pi/3$  ( $m$  odd) about the  $z$ -axis, to that for  $1/r_0$  with  $\theta = 0$ . In particular, equation (A.4b) now simplifies to

$$a = 4GK'(k) \quad (\text{A.8})$$

taken with  $\omega_n = r_0$  in equation (A.2). On inverting  $r_0$ , the only change to equation (A.8) is the replacement of  $K'$  with  $K$ . The vertical axis length  $c$ , in equation (A.5b), can also be rewritten in terms of purely real quantities using the reciprocal modulus transformation [46], giving

$$c = 4G_r K'(k_r) \quad (\text{A.9})$$

where

$$k_r = 1/k_z = ((r_0^6 + 1)^{1/2} - r_0^3)^2, \\ G_r = \{r_0^3/(r_0^6 + 1)\}^{1/2}(1 + k_r). \quad (\text{A.10})$$

Moreover, inverting  $r_0$  again corresponds to interchange of  $K'$  and  $K$ , now together with replacement of the factor of 4 by 8, in equation (A.9). Finally, for the  $rPD$  surface area, this special case of equations (A.6, A.7) with  $\phi_0 = 0$  simplifies to

$$S_p = \frac{4}{3} \int_0^1 dr (1+r^2)^2 \frac{1}{(r^3 + r_0^3)(r^3 + r_0^{-3})} \\ \times K' \left( \frac{|(r^3 - r_0^3)(r^3 - r_0^{-3})|}{(r^3 + r_0^3)(r^3 + r_0^{-3})} \right) \quad (\text{A.11})$$

and is clearly invariant under inversion of  $r_0$ .

## Appendix B: Parametrization of the tetragonal surfaces

The parametrization in equation (2), with  $R$  now supplied by equation (9), can be readily recast into standard elliptic integrals (the basic transformations have been long established [29] and recently re-analysed by Cvijovic and Klinowski [47]). Below we focus on the constraints and the resulting geometrical characteristics for the three families,  $tG$ ,  $tD$  and  $tP$ .

The tetragonal degradation of the cubic gyroid to the space-group  $I4_1/acd$  requires a commensurability condition in both the  $(x, y)$  and  $z$  directions. We phrase these conditions in terms of the positions of the surface-embedded inversion centers ( $\bar{1}$ ), relative to the origin  $\omega = 0$  at the  $\bar{4}$  site. The center corresponding to the parameter value  $\omega = \omega_0$  must satisfy  $y(\omega_0) = 0$ . From this first constraint on  $\theta$  the horizontal dimension  $a$  of the unit cell is expressed in terms of  $\omega_0$  via  $x(\omega_0) = a/4$ , giving

$$\tan \theta = \text{Re}\{iG_T K(k_T)\}/\text{Im}\{iG_T K(k_T)\} \quad (\text{B.1a})$$

$$a = 2\sqrt{2}|G_T|\text{Re}\{K(k_T)K'(k_T)^*\}/|K(k_T)| \quad (\text{B.1b})$$

where the modulus  $k_T$  and prefactor  $G_T$  are

$$k_T^2 = 1/2 + (\omega_0^{-2} + \omega_0^2)^{-1}, \\ G_T = (\omega_0^{-2} + \omega_0^2)^{-1/2}. \quad (\text{B.2})$$

Equivalently, one could switch the  $\omega_0$  in equation (B.2) to  $e^{i\pi/4}\omega_0$  and simultaneously replace  $K$  by  $iK - K'$  throughout equation (B.1) (now removing the  $\sqrt{2}$  factor from  $a$ ). The second constraint enforces the  $z$  lock-in and also supplies a formula for the vertical dimension  $c$  of the cell. Specifically we require that the height  $z(\omega_0) = c/8$

be consistent with that of the other center  $z(e^{-i\pi/2}\omega_0^{-1}) = 3c/8$ , giving

$\tan \theta =$

$$\text{Re}\{iG_{Tz}(K(k_{Tz}) + iK'(k_{Tz}))\} / \text{Im}\{iG_{Tz}(K(k_{Tz}) + iK'(k_{Tz}))\} \quad (\text{B.3a})$$

$$c = 8|G_{Tz}|\text{Re}\{K(k_{Tz})K'(k_{Tz})^*\} / |K(k_{Tz}) + iK'(k_{Tz})| \quad (\text{B.3b})$$

where the modulus and prefactor are now defined as

$$\begin{aligned} k_{Tz} &= (\omega_0^{-2} + \omega_0^2) / (\omega_0^{-2} - \omega_0^2), \\ G_{Tz} &= (\omega_0^{-2} - \omega_0^2)^{-1}. \end{aligned} \quad (\text{B.4})$$

We adopt the argument  $\phi_0$  as the independent variable indexing these  $tG$  surfaces, with their family spanning the range  $-\pi/2 < \phi_0 < 0$ . The corresponding  $r_0$  is obtained by equating equation (B.1a) to equation (B.3a); the remaining equations then specify the Bonnet angle and cell dimensions in terms of  $\phi_0$ .

The area  $S_p$  of the representative surface piece generated by the wedge region  $-\pi/4 \leq \phi \leq \pi/4$ ,  $0 \leq r \leq 1$ , is given by polar integration of equation (3a), and can be expressed elliptically as

$$S_p = \int_0^1 dr r (1+r^2)^2 |(r^8 - r_0^8)(r^8 - r_0^{-8})g|^{-1/2} K'(1/g) \quad (\text{B.5})$$

where  $g$  is again defined by equation (A.7), now with  $r^3$  replaced by  $ir^4$  (similarly for  $r_0$ ) and  $3\phi_0$  replaced by  $4\phi_0$ . The homogeneity index is defined in terms of the above quantities by

$$\mathcal{H} = N\sqrt{2/\pi}S_p^{3/2}/(a^2c) \quad (\text{B.6})$$

where  $N$  is the number of such surface pieces comprising the translational unit cell, so  $N = 32$  for  $tG$ . The surface average of an arbitrary power  $q$  of the local Gaussian curvature magnitude (see Eq. (3)), expressed in normalized form, is

$$\mu_q = \langle |K|^q \rangle / \langle |K| \rangle^q = (2/\pi)^q S_p^{q-1} \int (-K)^q dS_p. \quad (\text{B.7})$$

The  $tD$  family emerges continuously from the endpoint  $\phi_0 = 0$  (with  $\theta = 0$ ) of the  $tG$  family, with  $r_0$  now free to run over the range  $0 < r_0 < 1$ . The  $tD$  surface quantities, as functions of  $r_0$ , then follow immediately from this special case of the formalism above. It only remains to switch from the space-group  $I4_1/acd$  to the true symmetry  $P4_2/nnm$  for  $tD$  by dividing the resulting  $a$  and  $c$  by  $\sqrt{2}$  and 2, respectively. This then gives

$$a = 2G_T K'(k_T) \quad (\text{B.8a})$$

(with  $\omega_0 = r_0$  in Eq. (B.2)) and

$$c = 4(r_0^{-2} + r_0^2)^{-1} K [2(r_0^{-2} + r_0^2)^{-1}]. \quad (\text{B.8b})$$

Further, the general equation (B.5) for  $S_p$  simplifies by symmetry to

$$\begin{aligned} S_p &= \int_0^1 dr r (1+r^2)^2 \frac{1}{(r_0^4 + r^4)(r_0^{-4} - r^4)} \\ &\times K' \left( \frac{|(r_0^4 - r^4)(r_0^{-4} + r^4)|}{(r_0^4 + r^4)(r_0^{-4} - r^4)} \right) \end{aligned} \quad (\text{B.9})$$

and the value of  $N$  for the homogeneity index in equation (B.6) is now 8.

The  $tP$  family is adjoint to  $tD$ , *i.e.* only differs in the replacement of  $\theta = 0$  by  $\theta = \pi/2$ . Accordingly the quantities  $S_p$  and  $\mu_q$ , again as functions of  $r_0$ , are exactly as for  $tD$  above. For the  $tP$  space-group  $I4/mmm$  16 such pieces build the unit cell. The dimensions  $a$  and  $c$  of this cell are simply obtained from their counterparts in equation (B.8) by taking the complement, *i.e.* interchanging  $K$  and  $K'$ .

## References

1. L.E. Scriven, *Nature* **263**, 123 (1976).
2. S.T. Hyde, B.W. Ninham, S. Andersson, Z. Blum, T. Landh, K. Larsson, S. Lidin, *The Language of Shape* (Elsevier, Amsterdam, 1997).
3. J. Charvolin, J.-F. Sadoc, *J. Phys. France* **48**, 1559 (1987); J.-F. Sadoc, J. Charvolin, *Acta Cryst. A* **45**, 10 (1989).
4. D.M. Anderson, S.M. Gruner, S. Leibler, *Proc. Natl. Acad. Sci. USA* **85**, 5364 (1988).
5. S.T. Hyde, *J. Phys. Coll. France, Suppl.* **51**, C7-209 (1990); S.T. Hyde, *Curr. Opinion Solid State Mat. Sci.* **1**, 653 (1996).
6. V. Luzzati, P. A. Speg, *Nature* **215**, 701 (1967); V. Luzzati, T. Gulik-Krzywicki, A. Tardieu, *Nature* **218**, 1031 (1968); V. Luzzati, *J. Phys. France II* **5** (1995) 1649; V. Luzzati, H. Delacroix, A. Gulik, T. Gulik-Krzywicki, P. Mariani, R. Vargas, *Current Topics in Membranes* (Academic Press, 1997), p.3.
7. J.M. Seddon, R.H. Templar, *Phil. Trans. Roy. Soc. Lond. A* **344**, 377 (1993).
8. P. Barois, S.T. Hyde, B.W. Ninham, T. Dowling, *Langmuir* **6**, 1136 (1990).
9. C.T. Kresge, M.E. Leonowicz, W.J. Roth, J.C. Vartuli, J.S. Beck, *Nature* **359**, 710 (1992).
10. G.S. Attard, C.G. Göltner, J.M. Corker, S. Henke, R.H. Templar, *Angew. Chem. Int. Ed. Engl.* **36**, 1315 (1997).
11. Q. Huo, D. Margolese, U. Ciesla, P. Feng, T. Gier, P. Sieger, R. Leon, P. Petroff, F. Schüth, G. Stucky, *Nature* **368**, 317 (1994).
12. S. Inagaki, A. Koiwai, N. Suzuki, Y. Fukushima, K. Kuroda, *Bull. Chem. Soc. Japan* **96**, 1449 (1996).
13. A.-M. Levelut, E. Hallouin, D. Bennemann, G. Heppke, D. Löttsch, *J. Phys. II France* **7**, 981 (1997).
14. B. Pansu, *J. Phys. II France* **5**, 573 (1995).
15. H. Hasegawa, H. Tanaka, T. Hashimoto, C. Han, *Macromol.* **20**, 2120 (1987).

16. E.L. Thomas, D.M. Anderson, C.S. Henkee, D. Hoffman, *Nature* **334**, 598 (1988).
17. H.-U. Nissen, *Science* **166**, 1150 (1969).
18. K. Larsson, *J. Phys. Chem.* **93**, 7304 (1989).
19. G. Porte, M. Delsanti, I. Billard, M. Skouri, J. Appell, J. Marignan, F. Debeauvais, *J. Phys. II France* **1**, 1101 (1991); M. Filali, G. Porte, J. Appell, P. Pfeuty, *J. Phys. II France* **4**, 349 (1994).
20. U. Olsson, H. Wennerström, *Adv. Colloid Interf. Sci.* **49**, 113 (1994); J. Daicic, U. Olsson, H. Wennerström, J. Jerke, P. Schurtenburger, *J. Phys. II France* **5**, 199 (1995).
21. S. T. Hyde, *Langmuir* **13**, 842 (1997).
22. K.M. McGrath, D.M. Dabbs, N. Yao, I.A. Aksay, S.M. Gruner, *Science* **277**, 552 (1997).
23. H. Jinnai, T. Koga, Y. Nishikawa, T. Hashimoto, S.T. Hyde, *Phys. Rev. Lett.* **78**, 2248 (1997).
24. E.J.W. Verwey, J.Th.G. Overbeek, *Theory of the Stability of Lyotropic Colloids* (Elsevier, Amsterdam, 1948).
25. W. Helfrich, *Z. Naturforsch.* **28c**, 693 (1973); W. Helfrich, *Z. Naturforsch.* **33a**, 305 (1978).
26. J. Daicic, A. Fogden, I. Carlsson, H. Wennerström, B. Jönsson, *Phys. Rev. E* **54**, 3984 (1996).
27. T. Odijk, *Langmuir* **8**, 1690 (1992); R.J. de Vries, *Phys. Rev. E* **56**, 1897 (1997).
28. P. Pieruschka, S. Marcelja, *J. Phys. II France* **2**, 235 (1992).
29. H.A. Schwarz, *Gesammelte Mathematische Abhandlungen* (Springer-Verlag, Berlin, 1890).
30. A.H. Schoen, *Infinite periodic minimal surfaces without self-intersections*, NASA Technical Report #D5541 (1970).
31. R. Bruinsma, *J. Phys. II France* **2**, 425 (1992).
32. W.H. Meeks, *Indiana U. Math. J.* **39**, 877 (1990).
33. C. Oguey, J.F. Sadoc, *J. Phys. I France* **3**, 839 (1993); C. Oguey, *Foams and Emulsions*, edited by J.F. Sadoc and N. Rivier (Kluwer Academic Publishers, Amsterdam, 1998).
34. A. Fogden, S.T. Hyde, *Acta Cryst. A* **48**, 442 (1992); A. Fogden, S.T. Hyde, *Acta Cryst. A* **48**, 575 (1992); A. Fogden, *Acta Cryst. A* **49**, 409 (1993); A. Fogden, *Z. Kristallogr.* **209**, 22 (1994).
35. A.D. Benedicto, D.F. O'Brien, *Macromol.* **30**, 3395 (1997).
36. D.C. Turner, Z.-G. Wang, S.M. Gruner, D.A. Mannock, R.N. McElhaney, *J. Phys. II France* **2**, 2039 (1992); R.H. Templer, D.C. Turner, P. Harper, J.M. Seddon, *J. Phys. II France* **5**, 1053 (1995).
37. E. Blackmore, G.J.T. Tiddy, *J. Chem. Soc. Faraday Trans. 2* **84**, 1115 (1988); T.A. Bleasdale, G.J.T. Tiddy, *The Structure, Dynamics and Equilibrium Properties of Colloidal Systems*, edited by E. Wyn-Jones (Kluwer Academic Publishers, Amsterdam, 1990), p. 397; P. Kekicheff, G.J.T. Tiddy, *J. Phys. Chem.* **93**, 2520 (1989).
38. A.S. Fogden, M. Stenkula, C.E. Fairhurst, M.C. Holmes, M.S. Leaver, *Prog. Colloid Polym. Sci.* **108**, 129 (1998).
39. T. Hashimoto, S. Koizumi, H. Hasegawa, T. Izumitani, S.T. Hyde, *Macromol.* **25**, 1433 (1992).
40. D.A. Hajduk, P.E. Harper, S.M. Gruner, C.C. Honeker, G. Kim, E.L. Thomas, L.J. Fetters, *Macromol.* **27**, 4063 (1994).
41. E. Koch, W. Fischer, *Acta Cryst. A* **46**, 33 (1990).
42. S. Lidin, S.T. Hyde, *J. Phys. France* **48**, 1585 (1987); S. Lidin, *J. Phys. France* **49**, 421 (1988).
43. A. Fogden, M. Haeberlein, S. Lidin, *J. Phys. I France* **3**, 2371 (1993).
44. S. Lidin, S. Larsson, *J. Chem. Soc. Faraday Trans.* **86**, 769 (1990).
45. H. Karcher, *Manuscripta Math.* **62**, 83 (1988).
46. P.F. Byrd, M.D. Friedman, *Handbook of Elliptic Integrals for Engineers and Physicists* (Springer-Verlag, Berlin, 1954).
47. D. Cvijovic, J. Klinowski, *J. Phys. I France* **2**, 137 (1992).